Stark effect and polarizability of graphene quantum dots

Thomas Garm Pedersen[*]

Department of Physics and Nanotechnology, Aalborg University, DK-9220 Aalborg Øst, Denmark
and Center for Nanostructured Graphene, DK-9220 Aalborg Øst, Denmark

The properties of graphene quantum dots can be manipulated via lateral electric fields. Treating electrons in such structures as confined massless Dirac fermions, we derive an analytical expression for the quadratic Stark shift valid for arbitrary angular momentum and quantum dot size. Moreover, we determine the perturbative regime, beyond which higher-order field effects are observed. The Dirac approach is validated by comparison with atomistic tight-binding simulations. Finally, we study the influence on the Stark effect of band gaps produced by, e.g., interaction with the substrate.

I. INTRODUCTION

External electric fields are frequently applied to tune or characterize the properties of nanoscale electronic structures. A prominent effect is the Stark shift of confined electronic states, which has been studied extensively in semiconducting nanostructures such as GaAs quantum wells [1] and CdSe quantum dots [2]. With the development of graphene technology a range of new device geometries has become available. In contrast to traditional nanostructures, graphene-based geometries are atomically thin, i.e., fully two-dimensional. Thus, several experimental and theoretical studies of planar graphene nanostructures, including nanoribbons [3,4], nanorings [5,6], and quantum dots or nanodots [5,7–22], have been reported. Such atomically thin structures are highly sensitive to nearby gates [11,15,18] or charged nanotips [20], as observed in, e.g., quantized transport [11,15].

Similar to atomic systems and semiconductor nanostructures, the electronic states of graphene quantum dots can be manipulated via the Stark effect. So far, no experimental reports of Stark shifts in graphene dots have been reported, but several theoretical investigations exist. Thus, electric-field control over state localization [23,24] as well as magnetic [25] and optical [26] properties has been suggested. These studies all employed atomistic approaches such as tight-binding [23,26] or density-functional theory [24,25]. While accurate, such methods are restricted to rather small structures, typically well below the size of experimental geometries. In contrast, the Dirac equation approach can handle arbitrarily large structures [7,8,12,14,22]. This approach relies on the fact that carriers in graphene behave as massless Dirac particles as long as the energy is close to the so-called Dirac point of the graphene band structure. We have previously successfully applied this approach to study a range of graphene nanostructures such as antidot lattices [27] and isolated rings, dots, and antidots [22,28].

In the present work, we apply the Dirac equation approach to graphene quantum dots in lateral external electric fields such as that illustrated in Fig. 1. We consider circular quantum dots since experimental samples are frequently roughly circular in shape [13,17,20,21]. To lowest order in the electric field F the field-induced Stark shift ΔE of a

particular state is quadratic in F, i.e., $\Delta E = -\frac{1}{2}\alpha F^2$, where α is the polarizability of the state. We demonstrate below that compact analytical expressions for the polarizability can be found for all states. Also, we investigate numerically the effect of large electric fields, for which the quadratic Stark shift is no longer applicable. Moreover, the Dirac approach is compared with atomistic tight-binding results for small structures, demonstrating good agreement between the different approaches. Finally, to include band gaps induced by, e.g., interactions with a substrate we consider quantum dots cut from "gapped graphene" and study the influence of gaps on the Stark shift.

II. THEORY

We consider a circular graphene quantum dot such as the one sketched in Fig. 1 in the presence of a lateral electric field $\vec{F}$. Dots etched from a large sheet using lithography, as opposed to, e.g., patterned hydrogen adsorption [29], are expected to provide strong electron confinement. We aim to describe a graphene quantum dot with ideal confinement using the usual Dirac equation. Hence, the eigenstates are two-component spinors, and ideal confinement is enforced by the infinite-mass-barrier boundary condition coupling the spinor components at the periphery [14,22,30]. It is convenient to normalize the radial coordinate r by the radius a. In this manner, the boundary is located at $r = 1$. Accordingly, the unperturbed Hamiltonian for the K valley reads

$$H_0 = \frac{\hbar v_F}{a}\begin{pmatrix} 0 & -ie^{-i\theta}\left(\partial_r - \frac{i}{r}\partial_\theta\right) \\ -ie^{i\theta}\left(\partial_r + \frac{i}{r}\partial_\theta\right) & 0 \end{pmatrix}. \quad (1)$$

Here, $v_F = 10^6$ m/s is the graphene Fermi velocity. Clearly, the characteristic energy is $\hbar v_F/a$. For the K' valley, the Hamiltonian is transposed but otherwise identical to Eq. (1). The unperturbed eigenstates of angular momentum m are of the form

$$\psi_m^{(0)} = \frac{1}{\sqrt{2\pi}}\begin{pmatrix} f_m(r)e^{im\theta} \\ ig_m(r)e^{i(m+1)\theta} \end{pmatrix}. \quad (2)$$

For a circular geometry, ideal (infinite-mass) confinement is implemented by the boundary condition $f_m(1) = g_m(1)$ [14,22,30]. Hence, for a state with energy E and writing $k = aE/(\hbar v_F)$, it follows that, in terms of Bessel functions
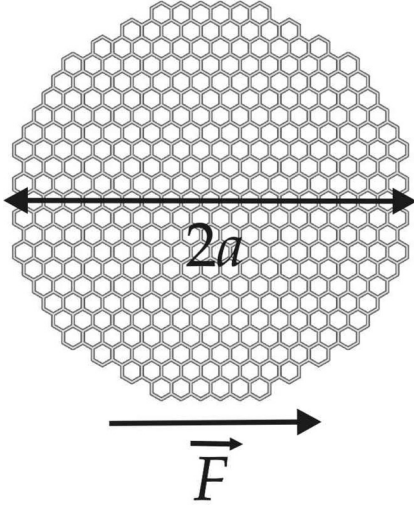

FIG. 1. Circular graphene quantum dot of radius a perturbed by a lateral electric field F.

J_m [12,14],

$$\begin{pmatrix} f_m(r) \\ g_m(r) \end{pmatrix} = N_m \begin{pmatrix} J_m(kr) \\ J_{m+1}(kr) \end{pmatrix},$$

$$N_m = \frac{1}{J_m(k)} \left(2 - \frac{2m+1}{k} \right)^{-1/2}, \quad (3)$$

with the additional condition $J_m(k) = J_{m+1}(k)$ due to the boundary condition. The parity conditions $J_{-m}(x) = (-1)^m J_m(x)$ and $J_m(-x) = (-1)^m J_m(x)$ ensure electron-hole symmetry of the energy spectrum. Moreover, the K' eigenstates are the transpose of the states above, and the energies are related via $E_m^{(K')} = -E_{m+1}^{(K)}$. The properties of the full spectrum of the two valleys are therefore identical up to a relabeling, and below we consider only the K valley.

In the presence of an external in-plane electric field F, the Hamiltonian is supplemented by the perturbation $H_1 = (\hbar v_F/a)\mathcal{E}r\cos\theta$, with $\mathcal{E} = eFa^2/(\hbar v_F)$. We are interested in the energy correction to second order in the field $E^{(2)}$ since the first-order correction vanishes due to inversion symmetry of the unperturbed system. Traditionally, $E^{(2)}$ has been calculated using second-order perturbation theory that involves an infinite sum over contributions. An extremely efficient and accurate alternative is the Dalgarno-Lewis perturbation theory [31], which has previously been applied to find polarizabilities of two-dimensional materials [32–34]. As a starting point, we consider the perturbed problem $(H_0 + H_1)\psi = E\psi$. Writing $\psi = \psi_m^{(0)} + \psi_m^{(1)} + \cdots$ as well as $E = E_m^{(0)} + E_m^{(2)} + \cdots$, where superscripts indicate the order of the perturbation, and collecting first-order terms, we must solve the inhomogeneous equation $(H_0 - E_m^{(0)})\psi_m^{(1)} = -H_1\psi_m^{(0)}$. In the present spinor problem, it can be demonstrated that the first-order correction can be written as

$$\psi_m^{(1)} = \mathcal{E} \frac{e^{im\theta}}{4\sqrt{2\pi}} \begin{pmatrix} e^{i\theta}F_m(r) + e^{-i\theta}\tilde{F}_m(r) \\ i[e^{2i\theta}G_m(r) + \tilde{G}_m(r)] \end{pmatrix}. \quad (4)$$

By collecting terms varying as $e^{\pm i\theta}$, the radial functions must satisfy

$$-kF_m(r) + G'_m(r) + \frac{m+2}{r}G_m(r) + 2rf_m(r) = 0,$$

$$-kG_m(r) - F'_m(r) + \frac{m+1}{r}F_m(r) + 2rg_m(r) = 0,$$

$$-k\tilde{F}_m(r) + \tilde{G}'_m(r) + \frac{m}{r}\tilde{G}_m(r) + 2rf_m(r) = 0,$$

$$-k\tilde{G}_m(r) - \tilde{F}'_m(r) + \frac{m-1}{r}\tilde{F}_m(r) + 2rg_m(r) = 0. \quad (5)$$

Similar to the unperturbed solutions, the boundary conditions for the first-order perturbation are $F_m(1) = G_m(1)$ and $\tilde{F}_m(1) = \tilde{G}_m(1)$. Combining homogeneous and particular solutions, it can be demonstrated that

$$F_m(r)/N_m = -\frac{2(m+1)}{k}rJ_m(kr) + (r^2-1)J_{m+1}(kr),$$

$$\tilde{F}_m(r)/N_m = r^2 J_{m+1}(kr) + J_{m-1}(kr),$$

$$G_m(r)/N_m = -r^2 J_m(kr) - J_{m+2}(kr),$$

$$\tilde{G}_m(r)/N_m = \frac{2m}{k}rJ_{m+1}(kr) - (r^2-1)J_m(kr). \quad (6)$$

Based on these results, we can now compute the second-order energy correction $E_m^{(2)}$ for a state of angular momentum m. In analogy with nonrelativistic (scalar) problems [32–34], the correction becomes

$$E_m^{(2)} = \langle \psi_m^{(0)} | H_1 | \psi_m^{(1)} \rangle = \frac{1}{8}\mathcal{E}^2 \int_0^1 \{f_m(r)[F_m(r) + \tilde{F}_m(r)]$$

$$+ g_m(r)[G_m(r) + \tilde{G}_m(r)]\}r^2 dr. \quad (7)$$

Hence, only the first-order correction to the wave function is required. It turns out that all integrals needed in Eq. (7) can be evaluated analytically. The final result can be written in the compact form

$$E_m^{(2)}(k) = \frac{1}{6k^2}\left\{-k + \frac{1}{2(2k-1-2m)} + \frac{m(m+1)}{k}\right\}. \quad (8)$$

The polarizability is then

$$\alpha_m(k) = \frac{1}{3k^2}\left\{k - \frac{1}{2(2k-1-2m)} - \frac{m(m+1)}{k}\right\}. \quad (9)$$

This important result has the expected $K \leftrightarrow K'$ symmetry $\alpha_m(k) = -\alpha_{-(m+1)}(-k)$.

The dimensionless polarizability in the massless Dirac model must be multiplied by $c_{\text{Dirac}} = e^2 a^3/(\hbar v_F)$ to obtain the physical, dimensionful quantity. In contrast, for nonrelativistic Schrödinger fermions, the corresponding factor is $c_{\text{Schrödinger}} = e^2 m_* a^4/\hbar^2$ [32–34], where m_* is the effective mass. Note the difference in scaling between the massless relativistic problem, for which the polarizability scales with size as a^3, and the nonrelativistic case scaling as $\alpha \propto a^4$. In the Dirac approach, massive rather than massless fermions can be studied by including mass terms $\pm\Delta$ in the diagonal of the Dirac Hamiltonian [12,22,27,28]. The mass term is related to the effective mass via $\Delta = m_* v_F^2$. Normalizing by the characteristic energy $\hbar v_F/a$, the relevant quantity becomes the
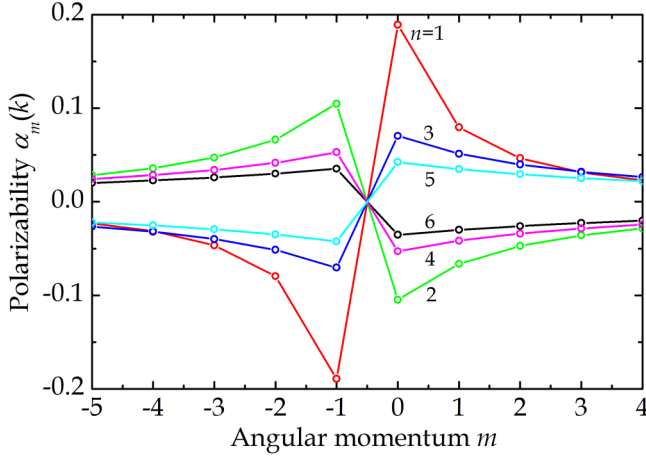
FIG. 2. Normalized polarizability for the lowest angular momenta and states around the Dirac point.

FIG. 3. Comparison of the approximate quadratic field dependence with the full numerical result.

normalized mass term $\delta = a\Delta/(\hbar v_F) = am_* v_F/\hbar$. Hence, we see that relativistic and nonrelativistic prefactors are related by $c_{\text{Schrödinger}} = \delta \cdot c_{\text{Dirac}}$.

Physically, a mass term describes a band gap of magnitude 2Δ in the energy spectrum. Band gaps can be caused by several effects such as interactions with substrates [35] or periodic gating [36]. Moreover, naturally gapped two-dimensional (2D) semiconductors such as h-BN or transition-metal dichalcogenides can be modeled using mass terms, i.e., differing on-site energies [37]. To include a possible mass term and also to study the transition from massless Dirac to massive Schrödinger cases, we include the massive (gapped) graphene model in the Appendix. The presence of mass terms complicates the expression for the correction to the wave function slightly [see Eq. (A3)]. However, an analytical expression for the polarizability can still be found, as shown in Eqs. (A4) and (A5). The general expression is clearly quite complicated. However, in the limit $\delta \gg 1$, we find the approximate result

$$\alpha_m(k) \approx \frac{(4 + k^2 - 4m^2)\delta}{6k^4}, \quad (10)$$

where k is now the root of the mth Bessel function $J_m(k) = 0$. For $m = 0$, this result agrees with the usual nonrelativistic expression $(4 + \lambda_2^2)\delta/(6\lambda_2^4)$, with $J_0(\lambda_2) = 0$ [34]. The factor of δ in Eq. (10) is precisely the expected manifestation of the nonrelativistic limit.

III. RESULTS

We now illustrate our results by evaluating Eq. (9) for the analytical polarizability for some important states in the vicinity of the Dirac point. To this end, we solve the eigenvalue condition $J_m(k) = J_{m+1}(k)$ for the unperturbed energies. Several eigenstates exist for any given m, and we use $n = 1, 2, 3, \ldots$ to distinguish these. Labeling states by $|m,n\rangle$ and writing k_{mn} for the associated wave number to make these quantum numbers explicit, we have for the lowest state $k_{01} \approx 1.435$ and, consequently, find from Eq. (9) $\alpha_0(k_{01}) \approx 0.189$. The polarizabilities for some low cases of m are plotted in Fig. 2, highlighting the symmetry $\alpha_m(k) = -\alpha_{-(m+1)}(-k)$. It is noted that $|\alpha_m(k)|$ decreases with $|m|$ but only slowly for
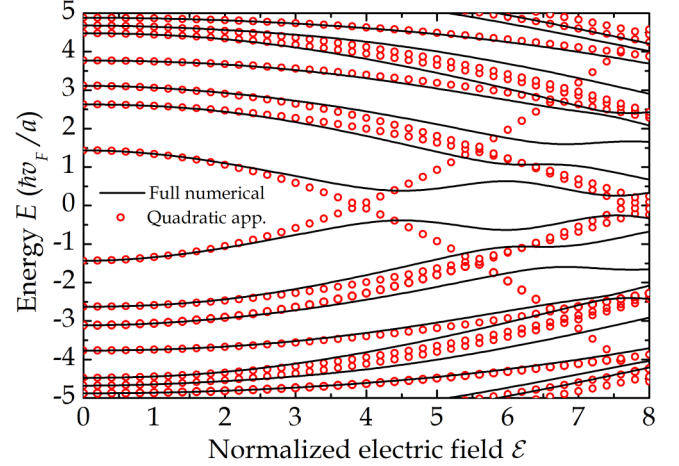
large angular momenta. Hence, the most polarizable states are the $|m = 0, n = 1\rangle$ and $|m = -1, n = 1\rangle$ ones.

To go beyond perturbation theory, we now consider the full problem $(H_0 + H_1)\psi = E\psi$ and expand the unknown wave function in a basis of unperturbed eigenstates $\psi_m^{(0)}$. We include angular momenta in the range $|m| \leqslant 10$ and, similarly, include the 20 states closest to the Dirac point for each m. This basis leads to converged results with absolute uncertainty below 10^{-5} in the energy range considered below. The results found by numerically diagonalizing the full Hamiltonian in this basis are compared to the analytical quadratic approximation in Fig. 3. Several features in this plot are worth stressing. Primarily, the quadratic approximation is in good agreement with the numerical curves for small field strengths, testifying to the correctness of the polarizability Eq. (9). Notice also the perfect electron-hole symmetry. Second, the perturbative regime extends up to field strengths of around $\mathcal{E} \approx 2$. Beyond this field, a much more complicated nonperturbative behavior is observed, including avoided crossings in several places. Finally, the states nearest to the Dirac point are seen to be most strongly affected by the field and are therefore the most polarizable.

Next, we wish to check the present approach against atomistic results. As explained above, atomistic approaches are highly reliable but limited to relatively small structures. Hence, we make the comparison for the four geometries inset in Fig. 4 that contain a manageable 780, 1728, 2076, and 4902 atoms, respectively. The atomistic calculation is made using the tight-binding (TB) method in the orthogonal nearest-neighbor approximation. We take the hopping integral $\gamma = 3.033$ eV [22,27] and bond length $a_{cc} = 1.42$ Å consistent with a Fermi velocity of $v_F = 10^6$ m/s. The circular quantum dots have radii a of $18.0a_{cc} \approx 26$ Å, $26.8a_{cc} \approx 38$ Å, and $29.4a_{cc} \approx 42$ Å, respectively, and the radius of the inscribed circle for the hexagonal one measures $43.0a_{cc} \approx 61$ Å. To find the Stark shift, a linearly varying electrostatic potential is added to the TB Hamiltonian. We take the field along either the zigzag x direction or armchair y direction. Hence, matrix elements $\Delta H_{nn} = eFx_n$ or $\Delta H_{nn} = eFy_n$ are added to the on-site energy of site n in the TB model.
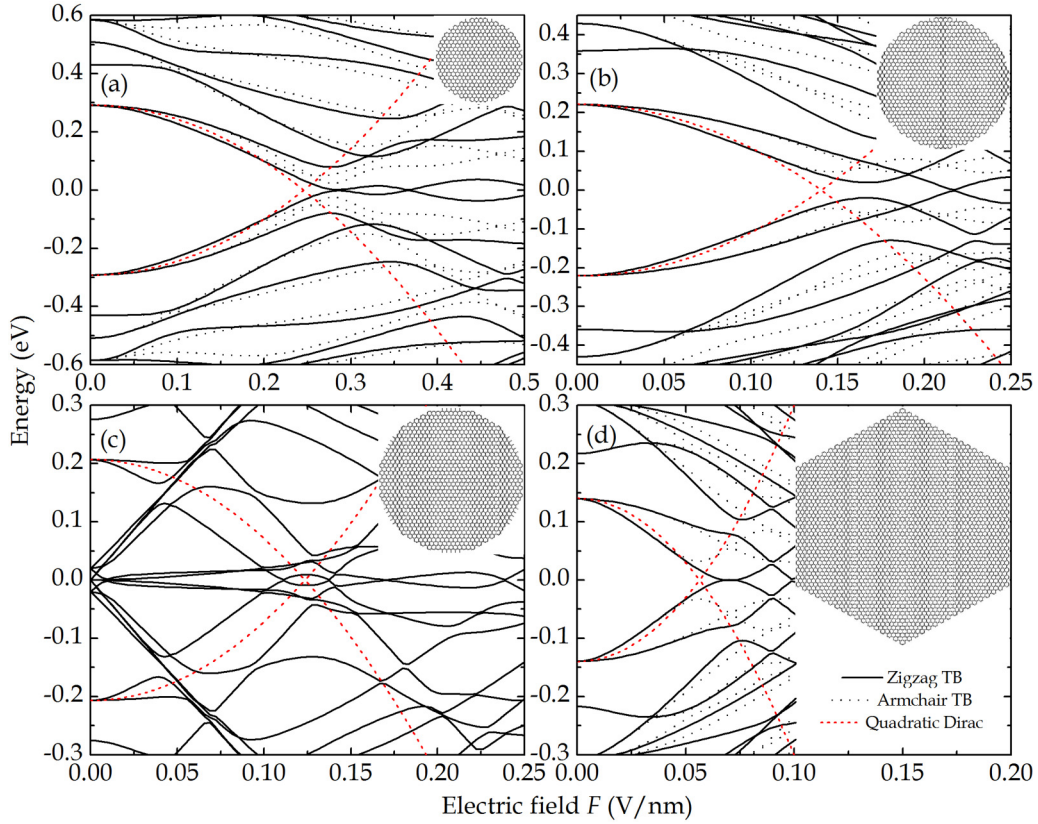
FIG. 4. Comparison of atomistic tight-binding results (solid and dotted black lines for x and y polarization, respectively) with the analytical quadratic approximation (dashed red lines) for four different quantum dot sizes. The radii are (a) 26, (b) 38, (c) 42, (d) and 61 Å, and the atomic geometries are shown in the insets.

The four geometries in Fig. 4 illustrate both the applicability and problems with the Dirac approach. In principle, the Dirac model is expected to be most accurate for low-energy states in relatively large structures, for which the continuum approximation holds. For large structures, however, complications due to edge states may appear, as discussed in detail below. Thus, the geometries in Figs. 4(a) and 4(b) represent relatively small or medium dots, whereas Fig. 4(c) is large enough to support extended zigzag edges. The hexagonal dot in Fig. 4(d) has exclusively armchair edges and hence does not support edge states. We include this noncircular geometry to demonstrate that the present model can, in fact, be successfully applied to such structures. In each circular dot, a state with energy E_{TB} between 0.2 and 0.3 eV is found in the TB model in the absence of the field. This state corresponds to the solution with Dirac energy $E_{01} = \hbar v_F k_{01}/a$ in the Dirac model. In fact, if the Dirac energy is calculated from the radius a used to define the atomic geometries, we consistently find energies that are slightly larger than the TB values. The physical reason is that the π-electron cloud in the TB model extends beyond the radius defining the atomic sites included in the geometry. Thus, a slightly larger effective radius a_{eff} might be applied to compensate for this discrepancy. To this end, we may simply determine a_{eff} by equating E_{TB} and $E_{01} = \hbar v_F k_{01}/a_{\text{eff}}$. Moreover, in this manner an effective radius for the hexagonal dot in Fig. 4(d) can be defined. This approach leads to the effective radii listed in Table I and shows that a_{eff} exceeds a by $\sim 4 - 7$ Å. In this manner, the TB and Dirac energies

in Fig. 4 are forced to coincide in the limit of vanishing field.

For finite fields, the plots in Fig. 4 illustrate the differences and similarities between TB and Dirac models. As shown by the solid and dotted lines, the atomistic results have a slight dependence on the orientation of the electric field. This is visible only for rather large fields, however, and the approximate quadratic behavior found in small fields is the same for both zigzag and armchair directions. Thus, the polarizability is independent of field orientation. The $|0,1\rangle$ states are twofold degenerate in the Dirac model due to valley degeneracy even in the presence of an electric field. From Fig. 4 it is seen that this degeneracy is lifted in the tight-binding simulation for finite field strengths. Thus, the state is split by the electric field, and accordingly, two separate

TABLE I. Characteristic parameters and polarizabilities for the four geometries in Fig. 4.

Structure	Fig. 4(a)	Fig. 4(b)	Fig. 4(c)	Fig. 4(d)
Radius a (Å)	25.6	38.1	41.7	61.0
TB energy E_{TB} (eV)	0.292	0.221	0.207	0.140
Eff. radius a_{eff} (Å)	32.3	42.7	45.5	67.3
α(eV nm^2/V^2)	9.67	22.4	27.1	88.1
$\alpha_{TB}^{(+)}$(eV nm^2/V^2)	13.3	29.2	60.4	110
$\alpha_{TB}^{(-)}$(eV nm^2/V^2)	7.25	12.9	7.53	35.9

polarizabilities describe the Stark effect. This feature is not captured in the Dirac model. Apart from this discrepancy, Figs. 4(a), 4(b), and 4(d) demonstrate good agreement between the Dirac model (based on effective radii) and the TB approach. Hence, even relatively small structures such as Fig. 4(a) can be described by the Dirac model if the effective radius is properly chosen. Moreover, it is gratifying that hexagonal geometries fit the model as such structures are typically found in dots grown by vapor deposition rather than defined by lithography. For the TB model, we extract numerical polarizabilities $\alpha_{TB}^{(\pm)}$ for the high- and low-energy state by fitting results for zigzag orientation to parabolas in the field range $|F| \leqslant 0.2 \, \text{V}/a$. Numerically, the polarizability in the Dirac model lies between the two atomistic values (see Table I). Also, focusing on the 38-Å structure in Fig. 4(b), the quadratic Stark shift model predicts a complete closing of the energy gap at field strengths around 0.17 V/nm, whereas the atomistic results predict an avoided crossing near 0.15–0.16 V/nm and a complete closing (for zigzag polarization) near 0.22 V/nm. Similar behavior is found in Figs. 4(a) and 4(d).

The 26- and 38-Å structures are small enough that no extended zigzag segments are found at the perimeter. Such segments lead to localized edge states with energy close to the Dirac point [27]. These effects cannot be captured by the Dirac approach used here, and hence, discrepancies between tight-binding and Dirac models are expected in such cases. To this end, we have included a somewhat larger geometry in Fig. 4(c). For clarity, only zigzag orientation of the field is shown. In this case, extended zigzag segments (with dangling bonded atoms) are found at the edge [see the geometry inset in Fig. 4(c)]. In the absence of an electric field, a total of 12 states are found close to the Dirac point with energy below $|E_{01}|$. In a finite field, the states split into three groups of four states each. One group of four states remains close to the Dirac point, whereas the remaining two either increase or decrease strongly with field depending on the sign of their dipole moment. Thus, these groups intersect the $|0,1\rangle$-type states at a finite field around 0.05 V/nm. This phenomenon is completely absent in the Dirac model. It can still be applied as an approximation for "bulk" states, however, in this case, and as shown in Fig. 4(d), it applies very well to large structures provided edge states are absent.

Finally, we address the gapped graphene case. As explained in the previous section and detailed in the Appendix, the presence of a band gap in the bulk of the graphene sheet can be incorporated via a mass term. Without additional confinement, this leads to the gapped graphene model that can be applied as a model of natural 2D semiconductors such as h-BN or transition-metal dichalcogenides. In the graphene case, a mass term can result from sublattice symmetry breaking via, e.g., interaction with a substrate [35]. Hence, the magnitude of the mass term may vary significantly between these different cases. In Fig. 5, the associated change in polarizability for some cases of low angular momentum and $n = 1$ is illustrated as a function of the normalized mass term δ using the gapped Dirac expressions (A4) and (A5). In all cases, the full calculation approaches the nonrelativistic limit as δ increases. However, rather large deviations are seen even for mass terms as large as $\delta = 50$. It is noted also that whereas the polarizability in the massless limit $\delta = 0$ remains positive for all $m \geqslant 0$, the
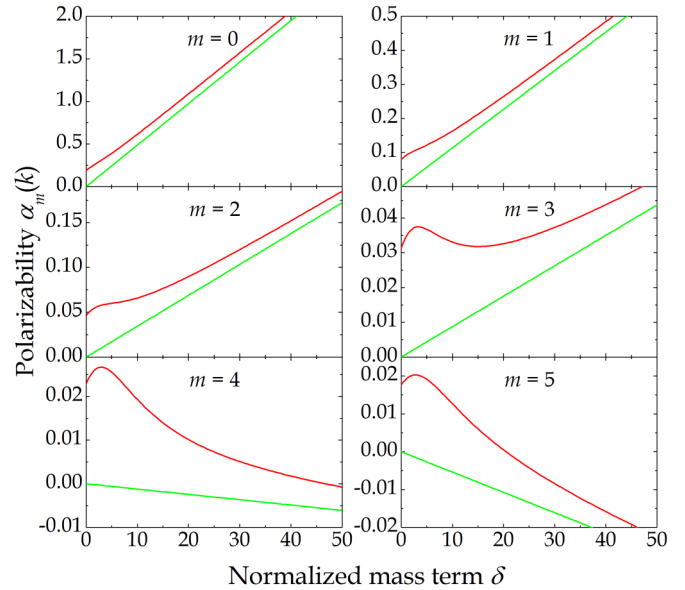

FIG. 5. Polarizability as a function of the mass term in gapped graphene quantum dots. The red and green lines are exact relativistic and approximate nonrelativistic values, respectively.

nonrelativistic cases turn negative for $m \geqslant 4$. When plotted against δ, the full polarizabilities therefore change sign at a certain value of δ for $m \geqslant 4$. We note that for $\Delta = 13 \, \text{meV}$ corresponding to the band gap of graphene on SiC substrates [35], a dot size of $a = 100 \, \text{nm}$ corresponds to a normalized mass parameter of only $\delta = a\Delta/(\hbar v_F) \approx 2$. Conversely, a similar disk of transition-metal dichalcogenide material with a band gap of $E_g \sim 2 \, \text{eV}$ has a mass term that is approximately 100 times larger. Hence, Fig. 5 shows that a small substrate-induced band gap has little effect on the Stark shift, whereas band gaps in the eV range will dramatically modify the Stark response of large dots.

IV. SUMMARY

In summary, a model based on the Dirac equation has been constructed for the Stark effect in graphene quantum dots. This makes it possible to treat arbitrarily large structures, in contrast to atomistic approaches. An analytical expression for the polarizability valid for arbitrary angular momentum and energy has been derived. Moreover, we have studied the high-field regime, for which the quadratic field dependence is no longer accurate. The Dirac model has been compared to an atomistic calculation of the Stark effect for small- and medium-sized dots to validate the results. Finally, the influence of a gap in the bulk graphene band structure due to, e.g., substrate effects has been investigated. We have found that typical gaps induced by substrates have a limited influence on the Stark shift.

APPENDIX: GAPPED GRAPHENE

The case of gapped graphene is slightly more involved than the gapless one but still analytically tractable. The modification is accomplished by adding mass terms $\pm\delta = \pm a m_* v_F/\hbar$ to the diagonal so that the unperturbed Hamiltonian for the K valley reads

$$H_0 = \frac{\hbar v_F}{a} \begin{pmatrix} \delta & -i e^{-i\theta}\left(\partial_r - \frac{i}{r}\partial_\theta\right) \\ -i e^{i\theta}\left(\partial_r + \frac{i}{r}\partial_\theta\right) & -\delta \end{pmatrix}. \tag{A1}$$

The eigenvalues are now $\varepsilon = \pm\sqrt{k^2 + \delta^2}$, and the eigenstates become

$$\begin{pmatrix} f_m(r) \\ g_m(r) \end{pmatrix} = N_m \begin{pmatrix} J_m(kr) \\ \frac{k}{\varepsilon+\delta} J_{m+1}(kr) \end{pmatrix}, \quad N_m = \frac{k}{J_m(k)}[\delta + \varepsilon(2\varepsilon - 2m - 1)]^{-1/2}. \tag{A2}$$

The quantization condition is then $J_m(k) = \frac{k}{\varepsilon+\delta} J_{m+1}(k)$. The Dalgarno-Lewis approach for the gapped case leads to a first-order correction that is still of the form of Eq. (4) but where

$$F_m(r)/N_m = \frac{2[\delta - (m+1)\varepsilon]}{k^2} r J_m(kr) + \frac{1}{k}\left(\frac{\delta}{m-\varepsilon+1} + \varepsilon(r^2 - 1)\right) J_{m+1}(kr),$$

$$\tilde{F}_m(r)/N_m = \frac{\varepsilon}{k} r^2 J_{m+1}(kr) + \frac{\delta + \varepsilon(\varepsilon - m)}{k(\varepsilon - m)} J_{m-1}(kr),$$

$$G_m(r)/N_m = -\frac{\varepsilon}{\delta + \varepsilon} r^2 J_m(kr) + \frac{\varepsilon(m - \varepsilon + 1) - \delta}{(\delta + \varepsilon)(-m + \varepsilon - 1)} J_{m+2}(kr),$$

$$\tilde{G}_m(r)/N_m = \frac{\delta - \varepsilon(\varepsilon - m)(r^2 - 1)}{(\delta + \varepsilon)(\varepsilon - m)} J_m(kr) + \frac{2(m\varepsilon - \delta)}{k(\delta + \varepsilon)} r J_{m+1}(kr). \tag{A3}$$

In turn, this leads to the rather cumbersome expression for the polarizability

$$\alpha_m(k) = \frac{1}{12k^4(\varepsilon - 1 - m)(\varepsilon - m)[\delta + \varepsilon(2\varepsilon - 2m - 1)]} \sum_{p=0}^{7} C_p \varepsilon^p, \tag{A4}$$

with coefficients

$$C_0 = (1 + 2m)\delta^2[4m^2(1+m)^2 - 2m(1+m)\delta - 2m(1+m)\delta^2 + 3\delta^3],$$

$$C_1 = -\delta\{24m^2(1+m)^2 - 6m(1+m)[1 - 4m(1+m)]\delta + [1 - 12m(1+m)]\delta^3 + 6\delta^4 - 2(\delta + 2m\delta)^2\},$$

$$C_2 = (1 + 2m)\{4m^2(1+m)^2 + 34m(1+m)\delta + 2[-5 + 9m(1+m)]\delta^2 - 5\delta^3 - 6\delta^4\},$$

$$C_3 = -6m(1+m)(1+2m)^2 - 2[5 + 32m(1+m)]\delta + [7 - 44m(1+m)]\delta^2 + 6\delta^3 + 4\delta^4,$$

$$C_4 = 2(1 + 2m)[1 + 4m(1+m) + \delta(5 + 9\delta)], \quad C_5 = 2[1 + 8m(1+m) - 6\delta^2], \quad C_6 = -12(1 + 2m), \quad C_7 = 8. \tag{A5}$$

[1] D. A. B. Miller, D. S. Chemla, T. C. Damen, A. C. Gossard, W. Wiegmann, T. H. Wood, and C. A. Burrus, Phys. Rev. Lett. **53**, 2173 (1984).

[2] F. Wang, J. Shan, M. A. Islam, I. P. Herman, M. Bonn, and T. F. Heinz, Nat. Mater. **5**, 861 (2006).

[3] X. Li, X. Wang, L. Zhang, S. Lee, and H. Dai, Science **319**, 1229 (2008).

[4] J. Cai, P. Ruffieux, R. Jaafar, M. Bieri, T. Braun, S. Blankenburg, M. Muoth, A. P. Seitsonen, M. Saleh, X. Feng, K. Müllen, and R. Fasel, Nature (London) **466**, 470 (2010).

[5] Z. Fang, S. Thongrattanasiri, A. Schlather, Z. Liu, L. Ma, Y. Wang, P. M. Ajayan, P. Nordlander, N. J. Halas, and F. J. García de Abajo, ACS Nano **7**, 2388 (2013).

[6] D. Cabosart, A. Felten, N. Reckinger, A. Iordanescu, S. Toussaint, S. Faniel, and B. Hackens, Nano Lett. **17**, 1344 (2017).

[7] B. Trauzettel, D. V. Bulaev, D. Loss, and G. Burkard, Nat. Phys. **3**, 192 (2007).

[8] P. G. Silvestrov and K. B. Efetov, Phys. Rev. Lett. **98**, 016802 (2007).

[9] L. A. Ponomarenko, F. Schedin, M. I. Katsnelson, R. Yang, E. W. Hill, K. S. Novoselov, and A. K. Geim, Science **320**, 356 (2008).

[10] A. Matulis and F. M. Peeters, Phys. Rev. B **77**, 115423 (2008).

[11] S. Schnez, F. Molitor, C. Stampfer, J. Güttinger, I. Shorubalko, T. Ihn, and K. Ensslin, Appl. Phys. Lett. **94**, 012107 (2009).

[12] N. M. R. Peres, J. N. B. Rodrigues, T. Stauber, and J. M. B. Lopes dos Santos, J. Phys. Condens. Matter **21**, 344202 (2009).

[13] H. G. Zhang, H. Hu, Y. Pan, J. H. Mao, M. Gao, H. M. Guo, S. X. Du, T. Greber, and H.-J. Gao, J. Phys. Condens. Matter **22**, 302001 (2010).

[14] M. Grujić, M. Zarenia, A. Chaves, M. Tadić, G. A. Farias, and F. M. Peeters, Phys. Rev. B **84**, 205441 (2011).

[15] J. Güttinger, F. Molitor, C. Stampfer, S. Schnez, A. Jacobsen, S. Dröscher, T. Ihn, and K. Ensslin, Rep. Prog. Phys. **75**, 126502 (2012).

[16] J. Shen, Y. Zhu, X. Yang, and C. Li, Chem. Commun. **48**, 3686 (2012).

[17] M. Li, W. Wu, W. Ren, H.-M. Cheng, N. Tang, W. Zhong, and Y. Du, Appl. Phys. Lett. **101**, 103107 (2011).

[18] C. Volk, C. Neumann, S. Kazarski, S. Fringes, S. Engels, F. Haupt, A. Müller, and C. Stampfer, Nat. Commun. **4**, 1753 (2013).

[19] A. El Fatimy, R. L. Myers-Ward, A. K. Boyd, K. M. Daniels, D. K. Gaskill, and P. Barbara, Nat. Nanotechnol. **11**, 335 (2016).

[20] J. Lee, D. Wong, J. Velasco, Jr., J. F. Rodriguez-Nieva, S. Kahn, H.-Z. Tsai, T. Taniguchi, K. Watanabe, A. Zettl, F. Wang, L. S. Levitov, and M. F. Crommie, Nat. Phys. **12**, 1032 (2016).

[21] C. Gutiérrez, L. Brown, C.-J. Kim, J. Park, and A. N. Pasupathy, Nat. Phys. **12**, 1069 (2016).

[22] M. R. Thomsen and T. G. Pedersen, Phys. Rev. B **95**, 235427 (2017).

[23] S. Evangelisti, G. L. Bendazzoli, and A. Monari, Theor. Chem. Acc. **126**, 257 (2010).

[24] A. D. Zdetsis and E. N. Economou, J. Phys. Chem. C **120**, 29463 (2016).

[25] L. A. Agapito, N. Kioussis, and E. Kaxiras, Phys. Rev. B **82**, 201411 (2010).

[26] Q.-R. Dong and C.-X. Liu, RSC Adv. **7**, 22771 (2017).

[27] M. Thomsen, S. J. Brun, and T. G. Pedersen, J. Phys. Condens. Matter **26**, 335301 (2014).

[28] J. G. Pedersen and T. G. Pedersen, Phys. Rev. B **85**, 035413 (2012).

[29] R. Balog, B. Jørgensen, L. Nilsson, M. Andersen, E. Rienks, M. Bianchi, M. Fanetti, E. Lægsgaard, A. Baraldi, S. Lizzit, Z. Sljivancanin, F. Besenbacher, B. Hammer, T. G. Pedersen, P. Hofmann, and L. Hornekær, Nat. Mater. **9**, 315 (2010).

[30] M. V. Berry and R. J. Mondragon, Proc. R. Soc. London, Ser. A **412**, 53 (1987).

[31] A. Dalgarno and J. T. Lewis, Proc. R. Soc. London, Ser. A **233**, 70 (1955).

[32] T. G. Pedersen, S. Latini, K. S. Thygesen, H. Mera, and B. K. Nikolic, New J. Phys. **18**, 073043 (2016).

[33] T. G. Pedersen, Phys. Rev. B **94**, 125424 (2016).

[34] T. G. Pedersen, New J. Phys. **19**, 043011 (2017).

[35] S. Y. Zhou, G. H. Gweon, A. V. Fedorov, P. N. First, W. A. De Heer, D. H. Lee, F. Guinea, A. H. Castro Neto, and A. Lanzara, Nat. Mater. **6**, 770 (2007).

[36] J. G. Pedersen and T. G. Pedersen, Phys. Rev. B **85**, 235432 (2012).

[37] T. G. Pedersen, Phys. Rev. B **92**, 235432 (2015).